EPS in press (2008/4/10)

Mapping the Upper Mantle Discontinuities beneath China with Teleseismic Receiver Functions

Xuzhang Shen [1, 2, 3] Huilan Zhou [1] and Hitoshi Kawakatsu[2]

1 Laboratory of Computational Geodynamics, Graduate University of the Chinese Academy of Sciences, Beijing, 100049, China
2 Earthquake Research Institute, University of Tokyo, 1-1-1 Yayoi, Bunkyo-ku, Tokyo 113-0032, Japan
3 Lanzhou Institute of Seismology, China Earthquake Administration, Lanzhou, 730000, China

We use teleseismic body waves recorded at stations of the Chinese Center of Digital Seismic Network to map the upper mantle discontinuities beneath China. Referring to the CRUST2.0 and a S-tomography model beneath each station, the 1-D ray tracing method is used to convert time series of radial receiver functions to depth series. Clear signatures corresponding to the 410- and 660-km discontinuities (‘410’ and ‘660’) are visible at almost all of the stations. The average S velocity contrast of ‘410’ beneath the study area is close to the global average, but for ‘660’, the S velocity contrast is smaller than the global average. The average depth of ‘410’ is 413 km, and the peak-to-peak topography is about 36 km, with regional depressions that correlate with the Datong quaternary volcano in north China. The ‘660’ topography exhibits peak-to-peak variation of about 43 km, and its average depth is 669 km; the depressions of the ‘660’ in northeastern, southeastern and northern China are well correlated with the past subduction around the Pacific Ocean and Philippine Sea. The width of the transition zone is also increased in the region with the deeper ‘660’. Our results seem to indicate that there may be a low velocity layer below ~600 km, which may be the accumulated garnetite layer of ancient crust above the ‘660’.

Key words: mantle discontinuity, China, receiver function, low velocity layer

1. Introduction

The subduction systems of the Pacific and Philippine Sea plates are located in the east of China, which cause island arcs, marginal seas and continental rift zones. Prior researches show that the western Pacific slab stagnates beneath the northeast of China (Fukao *et al*., 2001; Huang and Zhao, 2006) and might locally penetrate into the lower mantle (Li and Yuan, 2003). In the southwest of China, the Indian plate collides with the Eurasian plate, causing the Tibetan plateau with the highest mountain Himalaya and the thickest crust on the globe. The tomographic studies show the Datong quaternary volcano (DQV, Fig. 1) in north China may be related with the subducting Pacific slab (Zhao and Lei, 2004), and there may be a plume beneath the Hainan region (Lebedev and Nolet, 2003) in south China. Investigation of the topography of the upper mantle discontinuities can help us to better understand the evolution and dynamics of the slabs and to clarify the mechanism of volcanisms and plumes.

The receiver function (RF) method is an excellent tool for detecting seismic discontinuities in the upper mantle by analyzing P-to-S conversions (Langston, 1979). There are many case studies in the Chinese continent: the depth of the mantle discontinuities beneath China (Niu and Kawakatsu, 1998; Yang and Zhou, 2001), the lithospheric and upper mantle structure of southern Tibet (Yuan *et al*., 1997), a complex structure of the upper mantle discontinuities beneath northeastern China (Niu and Kawakatsu, 1996; Lebedev *et al*., 2002; Ai *et al*., 2003). Although these previous studies have obtained many important results, the resolution of the topography of the upper mantle discontinuities can be improved with the accumulation of recent observed data. In this work we analyze the receiver functions of 46 stations belonging to the Chinese Center of Digital Seismic Network (CCDSN). Referring to the CRUST2.0 model (Bassin *et al*., 2000) and the S-wave tomography model (Grand, 2002) beneath every station, time series of receiver functions are converted to depth series. The depths of the upper mantle discontinuities are obtained by analyzing these depth series. The results presented here are new

topography of the upper mantle discontinuities beneath whole continental China; compared to the earlier studies, new additional data were used, and regional earth models were referred to estimate the depth of the discontinuities.

2. Data

There are 48 broadband seismic stations belonging to the CCDSN; the average distance between two nearest stations is 500-600 km (Fig. 1). Due to the presence of failures in the equipment and other unknown reasons, records of stations NAQ in Tibet and XSA in southernmost China are not available. We collected records of Ms>5.5 teleseismic events from Nov. 2003 to Nov. 2005 with epicentral distances in the range between 30° and

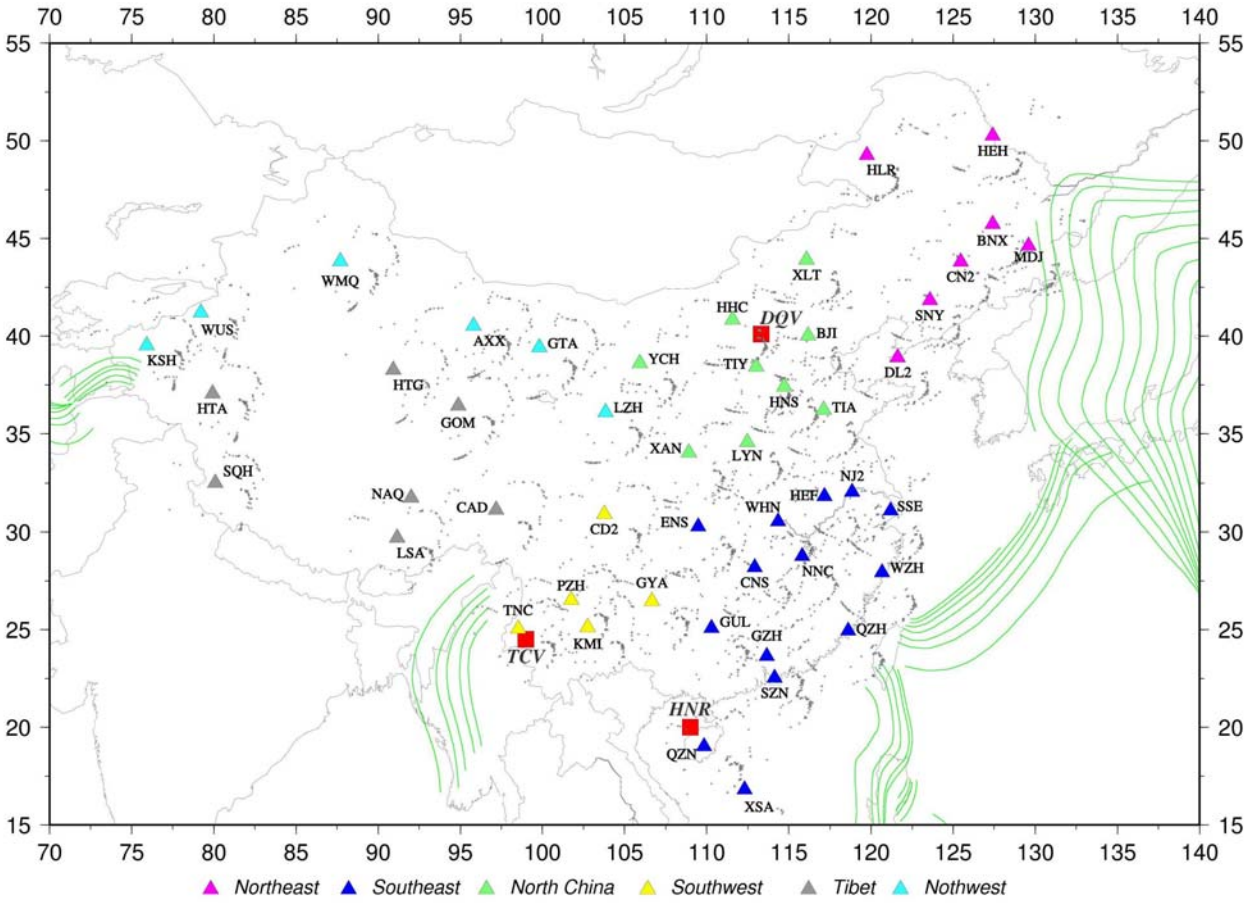

Fig 1. Location of stations and events. Triangles are location of stations, the letters beside them are names of stations, and the different color means that the station is in different regions. Squares represent the approximate location of volcanoes and a possible hot plume: DQV- Datong quaternary volcano, TCVs-Tengchong volcanoes, HNR-Hainan region (Lebedev and Nolet, *2003*). Green curves are contours of subducting slab around China (Gudmundsson and Sambridge, *1998*). Small black dots are the P660s pierce points of all ORFs. The distribution of earthquakes used in this paper is shown in the left bottom; triangle is the centroid location of the seismic network, and the red points are the event locations.

90°. We selected records that have decent signal-to-noise ratio and clear onset of the P-wave. Fig. 1 shows the locations of the stations, earthquakes and the entire pierce points of *P660s* (*Pds* refers to a P-to-S converted phase at a depth of *d km*) of the observed receiver functions (ORFs). The ORFs are calculated with the iterative deconvolution method in the time domain (Ligorria and Ammon, 1999), and a low-pass Gaussian filter with the half-width constant $\alpha = 1.5$ is applied; the corner frequency of the filter is 0.28Hz. In total, 4760 ORFs are used in our study.

3. Methodology

3.1 Moveout correction of receiver functions

A distance moveout correction for P-to-S converted phases is adapted (Yuan *et al*, 1997) to give prominence to Pds phases at each station. Based on the IASP91 model (Kennett and Engdahl., 1991), this correction shifts all the Pds phases to times of the same phases for an epicentral distance of 65°, The multiples can then be suppressed by stacking all the corrected ORFs. The bootstrap re-sampling method (Efron and Tibshirani, 1998) is used to estimate the error of the stacked results: the number of samples in each stacking equals to the number of ORFs, and the stacking is applied for 100 times to evaluate the standard deviation. The twice of the standard deviation, which gives the 95% confidence detection level, is used to show the stacked results.

3.2 Converting ORFs to the depth domain

The P-to-S converted phases of 410 and 660 km depths are clearly visible at most of the stations (Fig. 2a), which give a strong proof for the existence of these two upper mantle discontinuities beneath China. In order to determine the depth of the discontinuities, we attempt to correct the effect of the 3-D structure by referring to the CRUST2.0 model (Bassin *et al*., 2000) for both Vp and Vs of the crust; for the mantle, the 3-D shear velocity tomography model of Grand (Grand, 2002; Grand, 2006, personal communication) is referred as follows: (1) the average 1-D Vs model is taken from that of the Grand model, and then the average 1-D Vp model is constructed assuming the Vp/Vs ratio of IASP91. (2) Local 1-D Vs models beneath stations are constructed based on the Grand 3-D model. (3) Assuming that the local deviations are due to thermal anomaly, the local Vs anomalies are converted to the local Vp anomalies using the relation $R=dlnVs/dlnVp$ given by Karato (Karato, 1993; Karato, 2006, personal communication). (4) Local Vp anomalies are used to construct local 1-D Vp models.

The model is divided into thin layers; the thickness of the layers is 2 km in the crust, and 4 km in

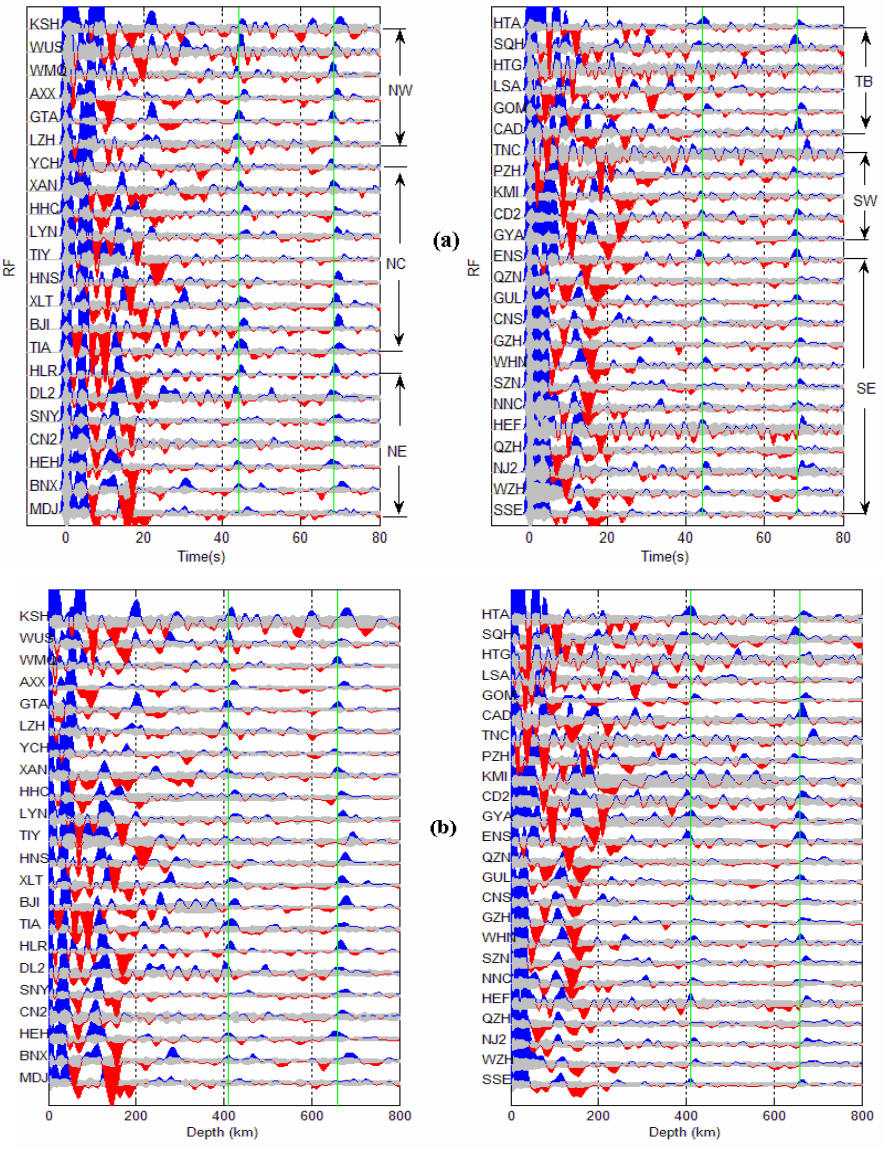

Fig 2. (a) Waveforms of the stacked moveout-corrected ORFs of every station. The gray shadow indicates the twice of the standard deviation estimated by the bootstrap method; the letters on the left are station codes, and the letters on the right represent the region (Fig.1) codes: NE-Northeast, NC-North China, NW-Northwest, SE-Southeast, SW-Southwest, TB-Tibet. The green lines show the expected timings of P410s and P660s predicted by IASP91; (b) Stacked results of converted depth series: the amplitude of the depth series is obtained from ORF (detailed explanations can be found in the text); the green lines show a depth of 410km and 660km.

the upper mantle. The travel times of P and Pds phases are calculated with the 1-D ray tracing method, and then the relative time of Pds phases of different depths to the P phase can be used to convert each time series (ORF) to a depth series. We average amplitudes before and after 0.3 s of the every ORF to construct the depth series (2-km and 4-km intervals for the crust and the upper mantle, respectively); this averaging time window of 0.6s corresponds an averaging depth of ~6km which is a little larger than the sampling intervals of the depth series; the procedure smoothes ORFs without losing information as 0.6s is below the corner period of the lowpass filter, and thus improves the stability of the results. The Pds phase signals could also be strengthened by stacking the depth series for each station, and the bootstrap method is still used to evaluate the error; Fig. 2b shows the depth series with error bounds for all the stations.

4. Results

The peaks near depths of 410 and 660 km are very clear for the most of stations (Fig.2b). The peaks near 410 km are ambiguous or multiples of shallower structures in some stations (MDJ, SNY, TIY, QZH, SZN, QZN, GUL, KMI, PZH, CAD and LSA), and the same for 660 km of stations MDJ, QZH and LSA. It is difficult to pick the depth of the discontinuities for these stations, so we do not attempt to do so. Table 1 lists the detailed depths of the 410 km and 660 km discontinuities (hereafter '410' and '660', respectively) observed at the stations which show clear signals. Fig. 3a and 3b show the topography of '410' and '660' respectively, and the thickness of the transition zone (H_{TZ}) are shown in Fig. 3c.

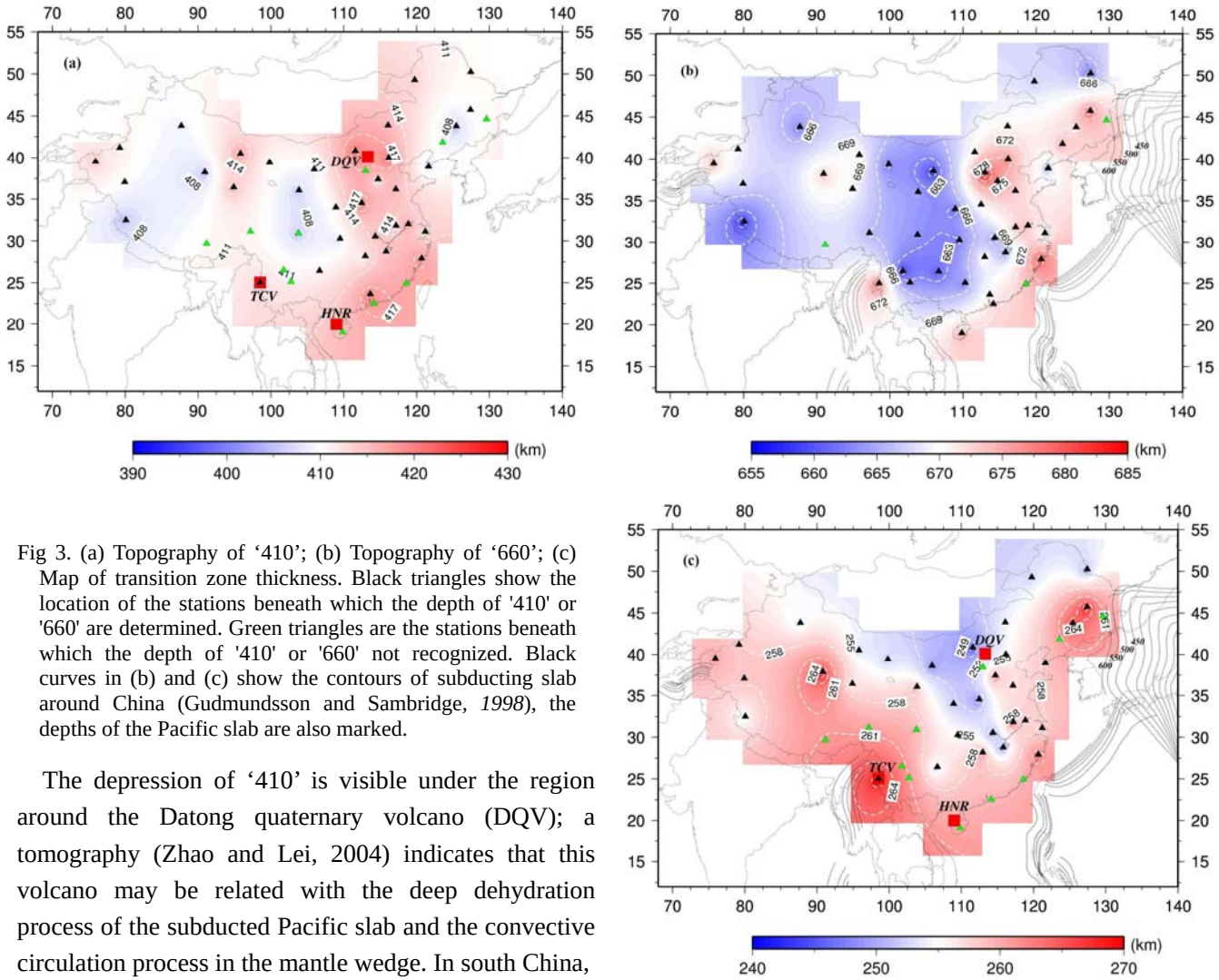

Fig 3. (a) Topography of '410'; (b) Topography of '660'; (c) Map of transition zone thickness. Black triangles show the location of the stations beneath which the depth of '410' or '660' are determined. Green triangles are the stations beneath which the depth of '410' or '660' not recognized. Black curves in (b) and (c) show the contours of subducting slab around China (Gudmundsson and Sambridge, *1998*), the depths of the Pacific slab are also marked.

The depression of '410' is visible under the region around the Datong quaternary volcano (DQV); a tomography (Zhao and Lei, 2004) indicates that this volcano may be related with the deep dehydration process of the subducted Pacific slab and the convective circulation process in the mantle wedge. In south China,

Table.1. Estimated depth of ‘410’ and ‘660’, R_{410}, R_{660} and thickness of transition zone

Station Code	Lon (°)	Lat (°)	‘410’ (km) (O	E)	R_{410}	‘660’ (km) (O	E)	R_{660}	H_{TZ}(km) (O	E)	N(evt)
AXX	95.800	40.514	423	1.5	0.031	674	2.4	0.030	251	3.4	140
BJI	116.168	40.018	425	2.5	0.047	679	2.0	0.058	254	3.4	126
BNX	127.405	45.740	410	3.3	0.035	685	5.1	0.042	275	6.2	75
CAD	97.500	31.000	----	----	----	664	2.0	0.088	----	----	88
CD2	103.758	30.910	403	3.2	0.046	664	2.0	0.048	261	6.2	90
CN2	125.448	43.801	402	5.5	0.025	671	5.0	0.033	269	8.2	62
CNS	112.931	28.182	409	2.2	0.033	675	8.8	0.021	266	10.8	86
DL2	121.628	38.906	404	2.0	0.052	662	7.6	0.035	258	7.4	107
ENS	109.487	30.272	405	3.2	0.054	660	3.1	0.060	255	3.5	122
GOM	94.873	36.432	419	3.4	0.032	672	1.9	0.039	253	3.8	109
GTA	99.814	39.411	409	2.4	0.045	660	2.2	0.043	251	3.5	156
GUL	110.294	25.076	----	----	----	659	3.0	0.036	----	----	90
GYA	106.664	26.459	411	4.0	0.040	658	3.0	0.049	247	4.3	112
GZH	113.344	23.087	424	6.6	0.023	670	7.0	0.028	670	7.1	91
HEF	117.168	31.836	410	2.7	0.043	675	6.7	0.046	265	7.3	69
HEH	127.410	50.250	410	6.1	0.025	655	6.1	0.029	245	6.4	107
HHC	111.564	40.849	427	6.7	0.031	668	1.5	0.025	241	7.2	138
HLR	119.740	49.267	415	1.8	0.055	666	1.1	0.059	251	2.1	131
HNS	114.708	37.418	409	4.1	0.018	677	1.8	0.047	268	5.8	121
HTA	79.917	37.067	411	3.5	0.083	670	3.9	0.042	259	4.6	61
HTG	90.760	37.860	400	3.5	0.035	677	6.3	0.024	277	8.5	97
KMI	102.740	25.123	----	----	----	663	4.0	0.034	----	----	116
KSH	75.923	39.517	417	3.3	0.056	680	5.3	0.078	263	8.2	100
LSA	91.150	29.700	----	----	----	----	----	----	----	----	116
LYN	112.468	34.550	428	6.6	0.019	671	1.9	0.038	243	6.5	114
LZH	103.844	36.087	403	3.8	0.048	666	3.6	0.030	263	4.5	118
MDJ	129.592	44.616	----	----	----	----	----	----	----	----	96
NJ2	118.854	32.052	419	2.6	0.036	675	9.9	0.031	256	5.8	78
NNC	115.801	28.778	415	4.7	0.025	660	7.6	0.022	245	11.5	77
PZH	101.743	26.504	----	----	----	649	6.8	0.048	----	----	113
QZH	118.592	24.943	----	----	----	----	----	----	----	----	94
QZN	109.843	19.029	----	----	----	677	6.9	0.023	----	----	93
SNY	123.578	41.828	----	----	----	677	6.1	0.026	----	----	123
SQH	80.080	32.500	401	9.5	0.035	650	2.7	0.070	249	12.0	80
SSE	121.187	31.096	410	2.5	0.032	665	2.0	0.019	255	3.0	112
SZN	114.080	22.320	----	----	----	673	2.2	0.039	----	----	88
TIA	117.124	36.211	417	5.9	0.046	673	6.9	0.030	256	9.1	115
TIY	113.017	38.430	----	----	----	693	2.4	0.036	----	----	122
TNC	98.520	25.029	414	6.9	0.037	690	2.1	0.057	276	7.2	101
WHN	114.350	30.544	416	4.9	0.048	661	1.5	0.046	245	5.0	98
WMQ	87.695	43.821	408	7.6	0.032	659	1.7	0.050	251	7.8	118
WUS	79.211	41.202	412	0.4	0.078	670	5.4	0.027	258	5.6	88
WZH	120.664	27.926	421	4.3	0.028	688	7.4	0.020	267	7.9	99
XAN	108.924	34.031	408	3.5	0.048	659	3.2	0.040	251	4.8	87
XLT	116.074	43.893	415	4.8	0.036	670	2.2	0.044	255	5.0	123
YCH	105.930	38.603	407	5.3	0.036	653	2.3	0.029	246	5.9	113

O: observed depth of ‘410’ and ‘660’; H_{TZ}: thickness of transition zone; E: error estimated by the boot strap method (two standard deviations); R_{410}: Amplitude ratio of $P_{410}s$ to P; R_{660}: Amplitude ration of $P_{660}s$ to P; N(evt): the number of events analyzed for the station; ----: the phase is ambiguous or multiples.

especially in south-western China, P410s is difficult to be picked in many stations (green triangles in Fig 3a). The tomography results show there is a low velocity zone between 238-410km in south-eastern China (Fukao et al, 2001), and even there may exist a plume originated from lower mantle beneath the Hainan region (HNR) (Lebedev and Nolet, 2003). On the other hand, the active Tengchong volcanoes (TCVs) are located in southwest of China. All of these results and phenomena seem to suggest a possible existence of high temperature region beneath these areas that may result in the complication of '410' in this area.

The '660' discontinuity is distinctly deeper than other regions in a triangle-like region in eastern China limited by the stations BNX, TIY and WZH, and this result is consistent with the previous results of receiver function analyses (Niu and Kawakatsu, 1998; Li and Yuan, 2003) and well correlated with the stagnant Pacific slab and Philippine Sea slab suggested by tomography (Fukao *et al*., 2001; Zhao and Lei, 2004; Huang and Zhao, 2006). The depths of '660' beneath TNC and KSH exceed 680 km, but these depressions are very local, and more dense data are needed to verify the results. In other area, the depths of '660' fluctuate within a narrow range.

From the results of H_{TZ} (Fig. 3c), the area with the obviously thicker transition zone in northeastern and eastern China is well correlated with the depression of '660' in the region, and this result further supports the existence of the stagnant Pacific and Philippine Sea slabs in this area. In the other regions, the variation of the thickness of the transition zone may only reflect local features because of the sparse station coverage, and thus we do not discuss about this further in the paper.

5. Discussion

Niu and Kawakatsu (1998) analyzed broadband seismic waveforms of 11 stations belonging to CDSN with polarized-filter to determine the absolute depths of the mantle transition zone discontinuities beneath China. Our results are basically consistent with theirs, but for BJI station, P410s and P660s of our ORF are very clear (Fig. 2(a)), and are consistent with Li *et al.* (2003). The complicated structure of '660' beneath MDJ has been suggested previously and interpreted differently (Niu and Kawakatsu, 1996; Lebedev *et al*., 2002; Ai *et al*., 2003). Our result also shows several weak peaks near a depth of 660 km, but as it is the stacking of ORFs from all directions, it does not allow us to discriminate the different models. A dense network observation, such as the proposed NECESSArray (NorthEast China Extended SeiSmic Array; planned by an international group of scientists of China-Japan-US) may be necessary for the purpose.

The amplitudes of converted phases of ORFs are mainly controlled by the velocity contrast of the discontinuities, but also depend on the epicenter distance (Ammon, 1991). Thus the amplitudes information can be distorted by directly stacking moveout-corrected ORFs of different epicenter distances. We corrected the amplitudes of ORFs approximately on the base of the transmission coefficient of P-to-S conversions of the IASP91 model for different distances before applying the moveout correction and stacking. Fig. 4 shows the amplitude ratio of *Pds* to *P* phases (R_d) beneath each station which is listed in Table 1. Although there is a large scatter in data, the averages of R_{410} and R_{660} are 3.98+-1.44% and 4.00+-1.55% in the study area, respectively. These two ratios are respectively 3.38% and 5.58% for synthetic RFs calculated for IASP91 with the PREM's Q model (Dziewonski and Anderson., 1981). This suggests that the S velocity contrast of the

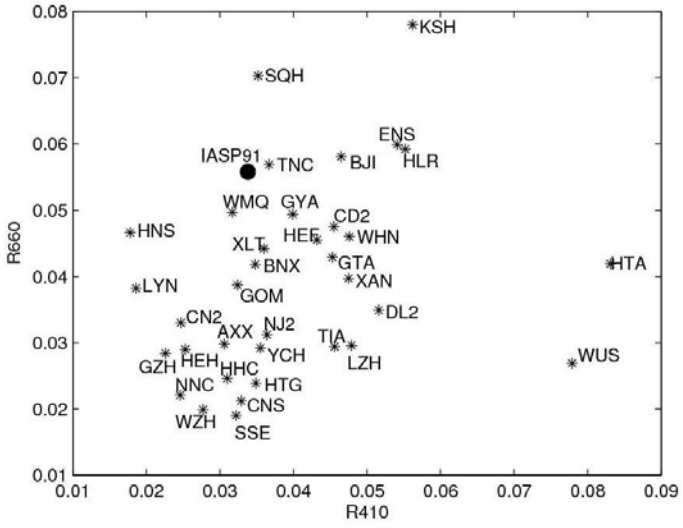

Fig 4. Amplitude ratios of P410s and P660s to P phase for each station. Circle shows the corresponding ratio of IASP91.

‘410’ beneath the study area is close to the global average, but that of the ‘660’ is small, although a part may be attributed to the lateral variation of the depth of ‘660’, because the distance of different pierce points of P660s is larger than P410s.

In addition to the P410s and P660s phases, we also noticed signatures above the noise level with a negative amplitude around 60s in many of the stacked ORFs (Fig. 2a). There are four possible explanations for a negative phase near 60s: (1) a P-to-S converted phase at a discontinuity of a depth of ~600km with a S velocity decease; (2) a first-order reverberation phase of a high velocity discontinuity at a depth of ~130km; (3) a first-order reverberation phase of a low velocity discontinuity at a depth of ~180km; (4) a second-order reverberation phase of a high velocity discontinuity at a depth of ~70km. For the second and third model, there should be corresponding positive and negative phases near the 15s and 20s respectively on ORFs; as we do not find these phases clearly in our results, these two possibilities are unlikely. In Tibet, the moho depth reaches to 70km (Bassin *et al.*, 2000), and it may produce a negative phase at ~60s. But in other regions, the first model is most likely to explain this negative phase.

In order to examine the regional characteristics of this negative phase signature before P660s, we divided the whole region into 6 parts (names of parts are listed in Fig. 2a). The moveout-stacked ORFs of each station (Fig 2a) are stacked straightly to produce average RFs of different regions (Fig. 5a), and also stacked aligned by the

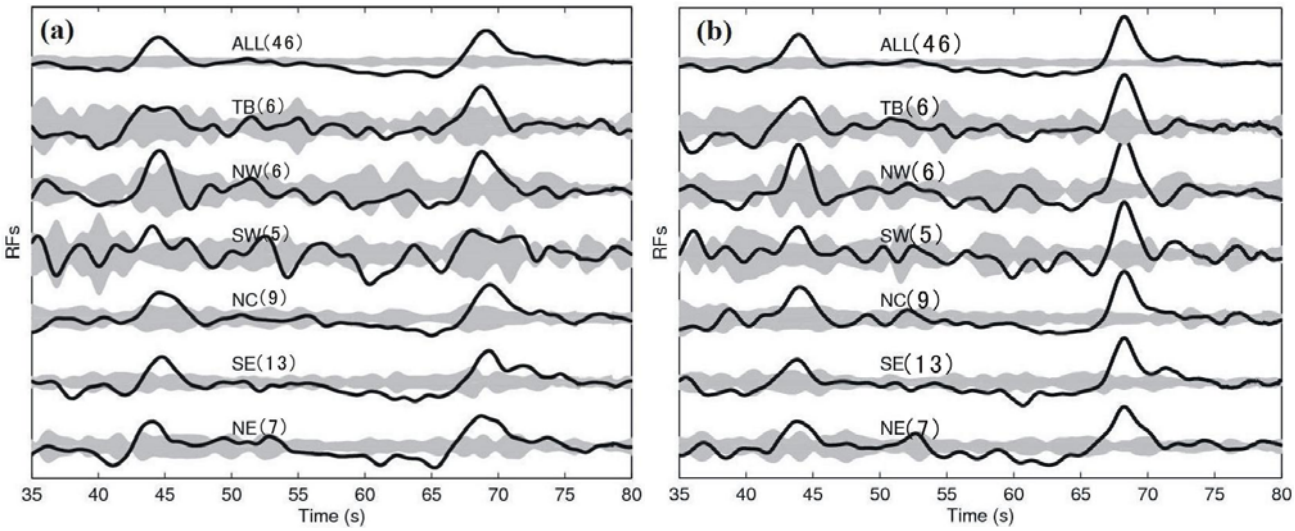

Fig 5. Regional averages of moveout-stacked ORFs of Fig 2a. (a) ORFs are stacked straightly: letters represent regions (with the number of stations), and 'ALL' indicates the average of all the stations; gray shadow represents the error (the 95% confidence level from bootstrap resampling method), and the bootstrap error estimates tend to over-estimate standard deviations for a small number of data. (b) ORFs are aligned by the peaks of the P660s phase and stacked.

P660s phases (Fig. 5b; the bootstrap method is used to estimate the error). In either of the cases, the negative phases or negative trends before *P660s* can be found in every region, so this negative phase signature appears to be not just a local but more general feature beneath China. In northeast China where the presence of the stagnant slabs are inferred (Fukao, 2001; Huang and Zhao, 2006), it is often observed that the fastest velocity anomalies are located in the middle of the transition rather than at the bottom; in such a region, this negative phase may correspond to the signature of the bottom boundary of the fast velocity stagnant slab. Such an interpretation, however, cannot explain that we observe similar negative phase signatures in other areas apparently ubiquitous beneath the Chinese continent.

We, therefore, suggest a hypothesis that there exists a low velocity layer (LVL) above the 660km discontinuity beneath the Chinese continent. Fig. 5a,b indicate that the times of the negative phases relative to the P660s may be quite variable in different regions, and so the thickness and property of the layer may be variable. A similar LVL was reported beneath southern Africa (Shen and Blum., 2003). They also observed a relatively small velocity contrast at ‘660’ beneath southern Africa as we found beneath China. They attributed it to the exsolution

of Ca-perovskite in former oceanic crust above the ‘660’ and the associated small volume fraction of ringwoodite there. The tomographic models and tectonic reconstructions show the ancient Tethys lithosphere thrusts beneath the Eurasia, and the slab detachment reached into the lower mantle (Hafkenscheid *et al*., 2006). The numerical simulations and theoretical analyses have shown that the oceanic crust may decouple from the subducted slab at the condition of ‘660’ (van Keken *et al*., 1996; Karato, 1997). So we tentatively suggest that the LVL observed ubiquitously beneath China may be a result of the accumulation of the Tethys crust (plus the Pacific crust). It may be also related with the accumulation of the delaminated continental crust (Karato, 2003). Further research is obviously needed to substantiate this hypothesis because the phases of LVL are not very strong.

6. Conclusion

We estimated depths of upper mantle discontinuities beneath China with teleseismic ORFs. There is a depression of ‘410’ around the Datong quaternary volcano; the depression of ‘660’ in eastern China are well consistent with the stagnating Pacific and Philippine-Sea slab as indicated by tomography and receiver functions. The contrast of S velocity of ‘410’ is close to the global earth average, while that of ‘660’ is smaller. Our result seems to indicate a possible presence of a low velocity layer above the 660 km discontinuity beneath the most of stations, which maybe explained by the accumulation of the ancient oceanic crust above the ‘660’ beneath China.

Acknowledgement. We are grateful to two anonymous reviewers for their detailed comments on the manuscript which improved it tremendously. This work is supported by the National Science Foundation of China (Grant 40574024 and 40374009). The part of the research was conducted while the first author was visiting at the Earthquake Research Institute, the University of Tokyo. The seismic wave data were supplied by China earthquake network center of Chinese Earthquake Administrator, Dr. Li and Dr. Yuan of GFZ gave help about the moveout of ORFs, and Dr. Zhang of GUCAS gave help about compute environment; Drs. Kumar and Tonegawa of ERI gave many helpful comments on the drafts. The authors gratefully acknowledge all of them.

References

Ai, Y., T. Zheng, W. Xu, Y. He and D. Dong, A complex 660kmn discontinuity beneath northeast China, *Earth. Planet. Sci. Lett*., 212, 63 -71, 2003.

Ammon, C.J., The isolation of receiver effects from teleseismic P waveforms, *Bull. Seismol. Soc. Am.*, 81: 2504–2510, 1991.

Bassin, C., G. Laske, and G. Masters, The current limits of resolution for surface wave tomography in North America, *EOS Trans. AGU*, 81, F897, 2000.

Dziewonski, A. M. and D. L. Anderson, Preliminary reference Earth model, *Phys. Earth. Planet. Inter.*, 25, 297-356, 1981.

Efron. B., and R. J. Tibshirani, An introduction to the Bootstrap, 436 pp., *Chapman & Hall*, 1998.

Fukao, Y., S. Widiyantoro, and M. Obayashi, Stagnant slabs in the upper and lower mantle transition region, *Rev. of Geophys.*, 39, 291-323, 2001.

Grand, S. P., Mantle shear-wave tomography and the fate of subducted slabs, *Phil. Trans. R. Soc. Lond. A*, 360, 2475-2491, 2002.

Gudmundsson, O., and M. Sambridge, A regionalized upper mantle (RUM) seismic model, *J Geophys Res,*. 103,7121-7136, 1998.

Huang, J., and D. Zhao, High-resolution mantle tomography of China and surrounding regions, *J. Geophys. Res.*, 111 B09305, doi:10.1029/2005JB004066, 2006.

Hafkenscheid, E., M. J. R. Wortel, and W. Spakman, Subduction history of the Tethyan region derived from seismic tomography and tectonic reconstructions, *J. Geophys. Res.*, 111, B08401, doi:10.1029/2005JB003791, 2006.

Karato, S., Importance of inelasticity in the interpretation of seismic tomography, *Geophys. Res. Lett*., 20, 1623-1626, 1993.

Karato, S., On the separation of crustal component from subducted oceanic lithosphere near the 660 km discontinuity, *Phys. Earth Planet. Inter.*, 99,103– 111, 1997.

Karato, S., The dynamic structure of the deep earth: an interdisciplinary approach, 241 pp., *Princeton Univ. Press*, Princeton and Oxford, 2003.

Kennett, B. L. N., and R. E. Engdahl, Travel times for global earthquake location and phase identification, *Geophys. J. Int.*, 105, 429–465, 1991.

Langston, C. A., Structure under Mount Rainier, Washington, inferred from teleseismic body waves, *J. Geophys. Res*., 84, B4, 4749-4762, 1979.

Lebedev, S., S. Chevrot, R. D. van der Hilst, The 660-km discontinuity within the subducting NW-Pacific lithospheric slab, *Earth. Planet. Sci. Lett*., 205, 25-35, 2002.

Lebedev, S., and G. Nolet, Upper mantle beneath Southeast Asia from S velocity tomography, *J. Geophys. Res*., 108, doi: 10.1029/2000JB000073, 2003.

Li, X., S. V. Sobolev, R. Kind, X. Yuan, C. H. Estabrook, A detailed receiver function image of the upper mantle discontinuities in the Japan subduction zone, *Earth. Planet. Sci. Lett*., 183, 527-541, 2000.

Li, X., and X. Yuan, Receiver functions in northeast China – implications for slab penetration into the lower mantle in northwest Pacific subduction zone, *Earth. Planet. Sci. Lett*., 216, 679 – 691, 2003.

Ligorria, J. P., and C. J. Ammon, Iterative deconvolution and receiver-function estimation, *Bull. Seismol. Soc. Am*., 89, 1395-1400, 1999.

Niu, F., and H. Kawakatsu, Complex structure of the mantle discontinuities at the tip of the subducting slab beneath the northeast China: a preliminary investigation of broadband receiver functions, *J. Phys. Earth*, 44, 701-711, 1996

Niu, F., and H. Kawakatsu, Determination of the absolute depths of the mantle transition zone discontinuities beneath China: effect of stagnant slabs on mantle transition zone discontinuities, *Earth, Planets and Space*, 50, 965-975, 1998.

Shen, Y., and J. Blum, Seismic evidence for accumulated oceanic crust above the 660-km discontinuity beneath southern Africa, *Geophys. Res. Lett.*, 30 (18), 1925, doi:10.1029/2003GL017991, 2003.

van Keken, P. E., S. Karato, and D. A. Yuen, Rheological control of oceanic crust separation in the transition zone, *Geophys. Res. Lett*., 23, 1821–1824, 1996.

Yang, Y., and H. Zhou, Application of receiver function method to estimate the buried depths of discontinuities in the upper mantle beneath china and adjacent area, *Chinese J . Geophys*., 44 (6) , 783-792, 2001.

Yuan, X., J. Ni, R. Kind, E. Sandvol, and J. Mechie, Lithospheric and upper mantle structure of southern Tibet from a seismological passive source experiment, *J. Geophys. Res.*, 102, B12, 27491-27500,1997.

Zhao, D., and J. Lei, Seismic ray path variations in a 3D global velocity model, *Phys. Earth. Planet. Inter.*, 141, 153 -166,2004.